PARTICLE CLUSTERING AND DEPOSITION OF POLYDISPERSE CLOUDS WITHIN ACCELERATING FLOW FIELDS

Denis Sotomayor-Zakharov
Institute of Fluid Mechanics (ISM)
Technische Universität Braunschweig
Hermann-Blenk-Str. 37, 38108 Braunschweig, Germany
d.sotomayor-zakharov@tu-braunschweig.de

Giuseppe A. Rosi, Mariachiara Gallia, David E. Rival
Institute of Fluid Mechanics (ISM)
Technische Universität Braunschweig
Hermann-Blenk-Str. 37, 38108 Braunschweig, Germany

ABSTRACT

The current study explores the influence of the flow field surrounding an immersed body on the freestream particle-size distribution of a disperse spray, as well as its effects on local particle clustering. The premise resides in visualizing the behavior of particles in a region with large flow acceleration, which results in particles of different sizes being deflected in different directions. For this, a test setup involving a wind tunnel with a water-spray nozzle is presented, on which a vertical flat plate was attached as the aerodynamic body in analysis, which generates the required accelerated flow field. Initial numerical simulations are carried in order to estimate the expected phenomena and to select a measurement window on the flow field. Experiments show indeed the expect behavior, where particles of small size are clustered and deflected away from the flat plate, while particles of large size remain parallel to the freestream. From the presented results, recommendations for future experimental tests are elaborated.

INTRODUCTION

Understanding mass-deposition onto immersed bodies in disperse particle-laden environments, such as droplet clouds or dust storms, requires a comprehensive understanding of both the impact mechanics of individual particles and their motions within the carrier phase. Investigating solid bodies immersed in a multiphase environment, such as a droplet cloud, necessitates a comprehensive understanding of particle motion and surface deposition. This understanding is crucial for various applications including cooling, surface treatment, particle separation and icing protection. The intrinsic qualities of the particles that determine their motions within the carrier phase are their density ρ_ϕ, which can typically be assumed constant across all particles, and their diameter ϕ, assuming perfect spheres. Unsurprisingly, ϕ determines the cumulative deposition of mass that appears on a immersed surface since it is essential to their motion within the carrier phase (Michaelides *et al.* (2022)). In a dusty flow over a planar surface, a cloud comprised of small particles will deposit less than a cloud comprised of larger particles, since large particles will ballistically impact the immersed surface while smaller particles will be carried with the flow. In the case of ice accretion of supercooled water droplets, the accretion process is mainly influenced by the droplets' size distribution and liquid water content in the cloud, as well as the freestream velocity.

In the above discussion, it has been implicitly assumed that cloud particles all have the same diameter. In reality, particle-laden environments are rarely mono-disperse and instead exhibit a particle-size distribution (PSD). The size distribution is not some afterthought, but instead has far-reaching significance on how it organizes particles within the cloud. How the size distribution affects the mass deposition onto a surface becomes clear with the following train of thought. Consider a cloud of polydisperse particles immersed in a horizontal flow impacting a sharp-edged flat plate oriented normal to the flow. Particles with a sufficiently small diameter ($\mathrm{Stk} \ll 1$) will follow the curvature and unsteadiness of the streamlines, thereby clustering within ensuing flow instabilities nearly perfectly, while larger particles will travel horizontally, practically unabated. As such, the PSD within the shear-layer region should skew heavily towards the smaller particles, which should faithfully follow the shear-layer motions, while shedding heavier particles. This reorganization of the cloud along inertial trajectories in accelerating flows has been observed in cylinder wakes (Yao *et al.*, 2009; Bagheri & Sabzpooshani, 2020), where inertial particles are depleted within the wake, as well as in vortical flows (Lacour *et al.*, 2011), which centrifuge inertial particles outward. Furthermore, in a manner that in non-monotonic with inertia, particles can potentially aggregate within regions or structures of the shear layer due to favorable interactions between the particles and the underlying wave feature, a phenomenon termed as "preferential sampling" (Monchaux *et al.*, 2012), or "phase locking" in the case of highly periodic fluid motions (Pushkin *et al.*, 2011). These thought experiments do not align neatly with the broad description provided earlier with regard to particle size and mass deposition, necessitating further investigation and experimentation.

To better understand how a PSD evolves in response to an unsteady flow, a series of experiments was conducted just above a shear layer formed by water-droplet-laden air clouds separating from a flat plate oriented normal to the airflow. The tests involved a wind tunnel equipped with a water spray nozzle, with the spray characterized using a shadowgraphy setup with high-speed cameras, from which particles can be tracked and sized using depth-from-defocus (DFD, Zhou *et al.* (2020); Xu *et al.* (2024)) imaging coupled with particle tracking velocimetry (PTV).

APPROACH FOR ANALYSIS

A fluid flow interacting with a body or obstacle develops regions of local acceleration or deceleration, which present a certain degree of influence over the dynamics of immersed particles. The force exerted on the particle can be modeled using the Maxey-Riley Equation (Eqn. 1, Maxey & Riley (1983)), for a spherical particle with diameter ϕ and velocity $u_{\phi,i}$ in the i direction. Here, μ_f represents the dynamic viscosity of the fluid, ρ_f the density of the fluid, ρ_ϕ the particle density, u_{f_i} the local fluid velocity, g_i the gravity acceleration, C_d the drag coefficient of the particle and Re_ϕ the particle Reynolds number. The term $F_{B,i}/m_\phi$ is a normalized force accounting for the history of the particle.

$$\begin{aligned}\left(1+\frac{1}{2}\frac{\rho_f}{\rho_\phi}\right)\frac{du_{\phi,i}}{dt} &= \underbrace{\frac{3}{2}\frac{\rho_f}{\rho_\phi}\frac{Du_{f,i}}{Dt}}_{\text{Fluid acceleration}} + \underbrace{\frac{3(C_dRe_\phi)\mu_f}{4\rho_\phi\phi^2}\left(u_{f,i}-u_{\phi,i}\right)}_{\text{Drag}} \\ &+ \underbrace{\left(1-\frac{\rho_f}{\rho_\phi}\right)g_i}_{\text{Gravity / buoyancy}} + \underbrace{\frac{F_{B,i}}{m_\phi}}_{\text{History term}}\end{aligned} \tag{1}$$

Following the previous equation, Re_ϕ is defined as:

$$Re_\phi = \frac{\rho_f|\vec{u}_f-\vec{u}_\phi|\phi}{\mu_f} \tag{2}$$

The Maxey-Riley Equation can be normalized using a freestream velocity U_∞ and a the lengthscale of the obstruction L. In doing so, the Stokes number (Stk) appears naturally from the dimensionalization, as well as the density ratio ($R=\rho_f/\rho_\phi$) and the Froude number ($Fr=U_\infty/\sqrt{gL}$):

$$\begin{aligned}\left(1+\frac{1}{2}R\right)\frac{d\tilde{u}_{\phi,i}}{d\tilde{t}} &= \underbrace{\frac{3}{2}R\frac{D\tilde{u}_{f,i}}{D\tilde{t}}}_{\text{Fluid acceleration}} + \underbrace{\frac{1}{Stk}(C_dRe_\phi)(\tilde{u}_{f,i}-\tilde{u}_{\phi,i})}_{\text{Drag}} \\ &+ \underbrace{(1-R)\frac{1}{Fr^2}e_{g,i}}_{\text{Gravity / buoyancy}} + \underbrace{\frac{1}{\sqrt{Stk}}\mathscr{H}_i}_{\text{History term}}\end{aligned} \tag{3}$$

Where Stk is defined as:

$$Stk = \frac{\rho_\phi U_\infty \phi^2}{18\mu_f L} \tag{4}$$

From Eqn. 3, it is evident that regions of the flow exhibiting strong spatial or temporal velocity gradients exert a significant influence on particle motion. In such regions, large fluid accelerations amplify the first term on the right-hand side, while the resulting slip between particle and fluid velocities enhances the drag term. Consequently, the present study focuses on regions near the shear layer, where these conditions are pronounced and are therefore expected to strongly influence particle dynamics.

EXPERIMENTAL SETUP

The experimental setup is shown in figure 1. Tests were performed in the Mobile Open Wind Tunnel (KFZ) of the ISM, which is equipped with a convergent duct that exits into a test section with 0.3 m x 0.3 m cross-sectional area and 1.5 m length. A flat plate of height $h=0.03$ m and thickness $t=0.01$ m was centered at 0.15 m from the bottom wall and a distance of 0.9 m from the duct exit. The KFZ can reach speeds up to 30 m/s and is equipped with a water spray nozzle located before the convergent duct, which generates a water-droplet cloud whose PSD is controlled by changing the pressures of both water and air flowing into the nozzle. Specifically, the manometric pressure of water p_w mainly dictates the amount of liquid water content LWC of the cloud, while the difference between the air pressure p_a and p_w regulates the mean-volume-diameter MVD of the PSD, with larger values of $\Delta p = p_w - p_a$ increasing the MVD.

At steady conditions, the flat plate generates two shear layers along its upper and lower edges, which shed into a von Kármán vortex street in the downstream wake. Tests were performed at a flow velocity of $U_\infty = 10\,$m/s, at a an ambient temperature of $T_\infty = 16\,^\circ$C and pressure of $P_\infty = 1\cdot 10^5$ Pa. This resulted in the flow properties shown in Table 1, with $Re_h = U_\infty h/\nu_\infty$. The test matrix is presented in Table 2 and consists of 4 test points, which cover large and small LWC and MVD. It is expected that variations in LWC and MVD may affect the quality of the computed particle properties across different particle sizes. However, since the carrier flow conditions are identical, the underlying particle dynamics for particles of the same diameter ϕ should remain consistent across all test cases.

A high-speed Phantom Camera T4040 and a 120W LED were aligned in the spanwise direction of the KFZ. The focal plane of the camera was positioned at the mid-span of the flat plate, while the field of view was centered at an $x=0$ m and $y=27$ mm from the middle of the flat plate, which is shown to be a location with high particle clustering based on numerical simulations of the particle dynamics; see next section. Images were sampled at 15 000 Hz, with an exposure time of 3 μs and a picture resolution of 2048 $\times$ 1024 pixels, resulting in a test window of 18 mm $\times$ 9 mm.

NUMERICAL SIMULATIONS

Numerical simulations of the present flow configuration were performed to determine the field-of-view location based on particle concentration (clustering), as well as to compute fields of relative particle velocity and local acceleration. The calculation of particle dynamics was done with the use of the DICEPS particle solver (Sotomayor-Zakharov & Bansmer, 2021; Sotomayor-Zakharov *et al.*, 2023), which takes the velocity fields calculated via ANSYS Fluent to solve for the trajectories of particles of different diameters ϕ. The flat plate inherently induces a von Kármán Vortex street, necessitating a

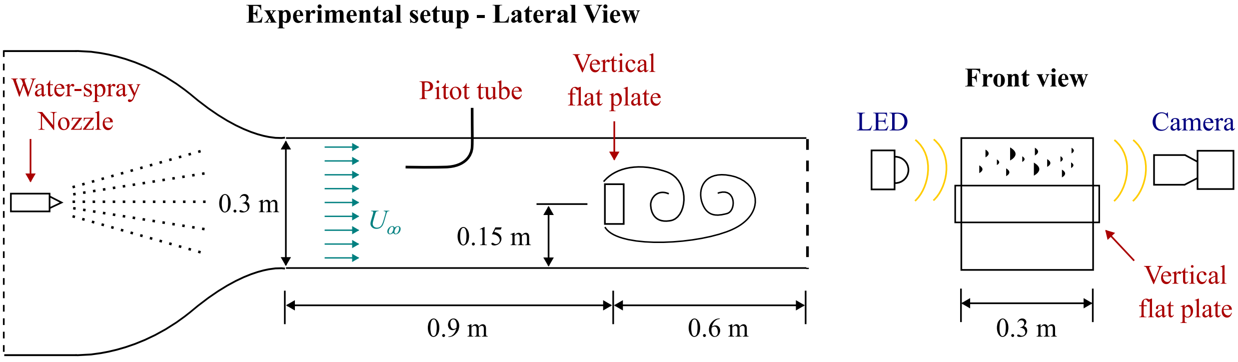

Figure 1. Experimental setup.

Table 1. Properties of the fluid flow.

Property	Unit	Magnitude
U_∞	m/s	10
ρ_∞	kg/m^3	1.22
ν_∞	m^2/s	$1.47 \cdot 10^{-5}$
Re_h	1	20 310
Fr^2	1	340
R	1	0.001

Table 2. Test matrix.

ID	p_w/P_∞	$\Delta p/p_w$	Comment
T1	4	0.50	Large LWC & Large MVD
T2	4	0.25	Large LWC & Small MVD
T3	2	0.50	Small LWC & Large MVD
T4	2	0.25	Small LWC & Small MVD

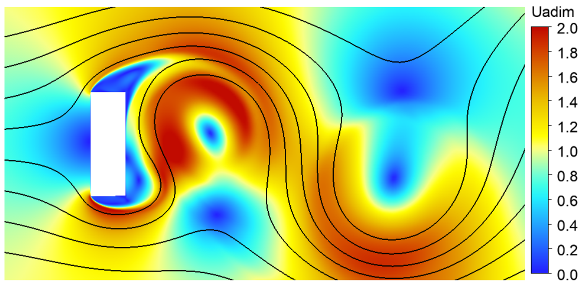

Figure 2. Instantaneous velocity $|u_f|/U_\infty$ and streamlines.

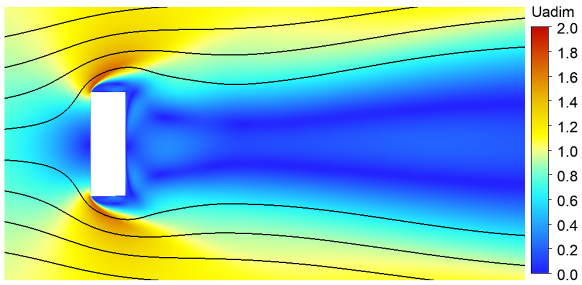

Figure 3. Averaged velocity $|\overline{u}_f|/U_\infty$ and streamlines.

URANS simulation approach with the properties of Table 1 as input parameters. The SST k-ω model was employed (Menter, 1994), as well as second-order schemes for spatial and temporal descriptions. The time-step used for the simulation was of $\Delta t = T_{osc}/64$, with $T_{osc} = h/(U_\infty Sth)$, with the Strouhal number $Sth = 0.2$. The relevant fields for analysis were averaged over a time $T_{avg} \approx 50T_{osc}$. Figure 2 and 3 display the result of such averaging, displaying a representative instantaneous velocity field and the averaged velocity field, respectively.

Since the particle solver uses an Eulerian approach, fields of particle velocity $\vec{u}_\phi$ are obtained for each particle diameter, as well as fields of particle concentration α_ϕ. Therefore, numerical simulations for particles with different ϕ were performed, with the particle properties presented in Table 3. It is noted that the particle solver uses the averaged velocity fields as input for the calculation of the particle dynamics, thereby disregarding the unsteady flow effects from the simulation.

Results of the particle concentration fields are presented in figures 4 and 5 for all particle sizes. Streamlines of the flow (black lines) and some particle trajectories (blue) are displayed as well on top of the fields. It can be seen that the region directly above and below the point of flow separation from the flat plate exhibits streamlines of high curvature, which exert a strong effect on the local particle concentration; this effect diminishes as particle size increases. Therefore, a field of view within this region was selected to investigate the reorganization of the particle cloud by the flow field as a function of particle size. Specifically, the FOV selected for the experiments is shown in Figure 6.

PARTICLE VISUALIZATION

Particle cloud images obtained following the test matrix of table 2 are presented in figure 7 and compared to the concentration fields of D2. The band of high concentration exhibited in the simulation generally coincides with that observed within the images.

The clustering predicted by the numerical simulations for the small particle sizes can be noted in the experimental results.

Table 3. Particle properties at different ϕ.

ID	ϕ	Re_ϕ	Stk
-	μm	1	1
D0	6	4	0.04
D1	12	8	0.15
D2	24	16	0.60
D3	48	33	2.4
D4	96	65	10
D5	192	131	38

Additionally, the effect of reducing MVD is noted when respectively comparing cases T1 and T3 to T2 and T4, with the angle with the horizontal of the concentration increasing with reduced MVD, indicative of smaller particles being more prone to follow streamlines. The effect of the reduced LWC can be seen between figures T1 and T3, with a reduction in shadowed regions indicative of the reduced amount of parti-

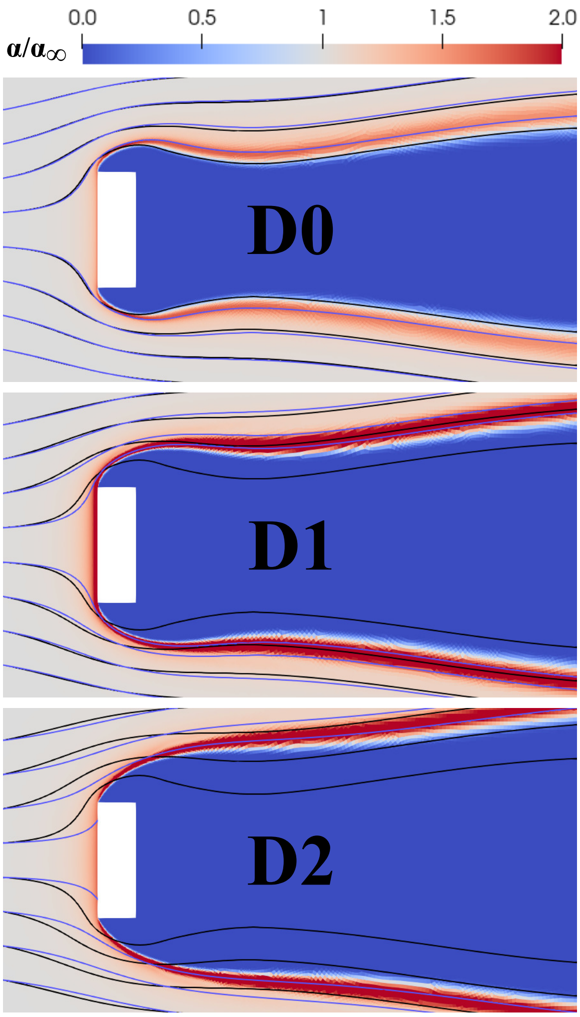

Figure 4. Fields of particle concentration for D0, D1 and D2. Flow streamlines (black lines) and particle trajectories (blue lines) are plotted as well.

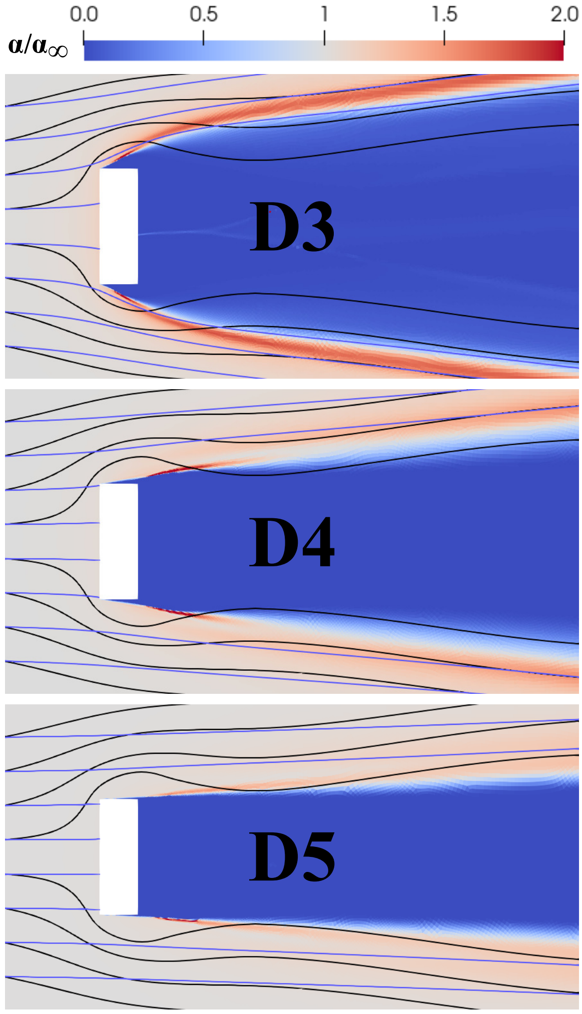

Figure 5. Fields of particle concentration for D3, D4 and D5. Flow streamlines (black lines) and particle trajectories (blue lines) are plotted as well.

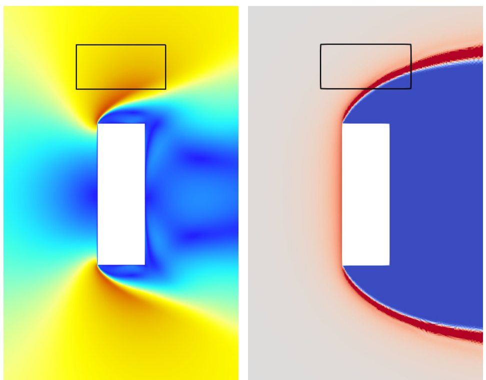

Figure 6. Location of test window based on numerical simulations. (a) Averaged velocity $|\overline{u}_f|/U_\infty$. (b) Fields of particle concentration for D2.

cles. Figures T2 and T4 do not display this effect in an obvious manner due to the large amount of existing particles.

It is worth noting how the von Kármán street forming downstream of the flat plate, which induces an oscillating behavior in the separated flow region on the top and bottom of the flat plate (see Fig. Fig. 2) affects particle motions within the concentrated regions captured in the images. Specifically,

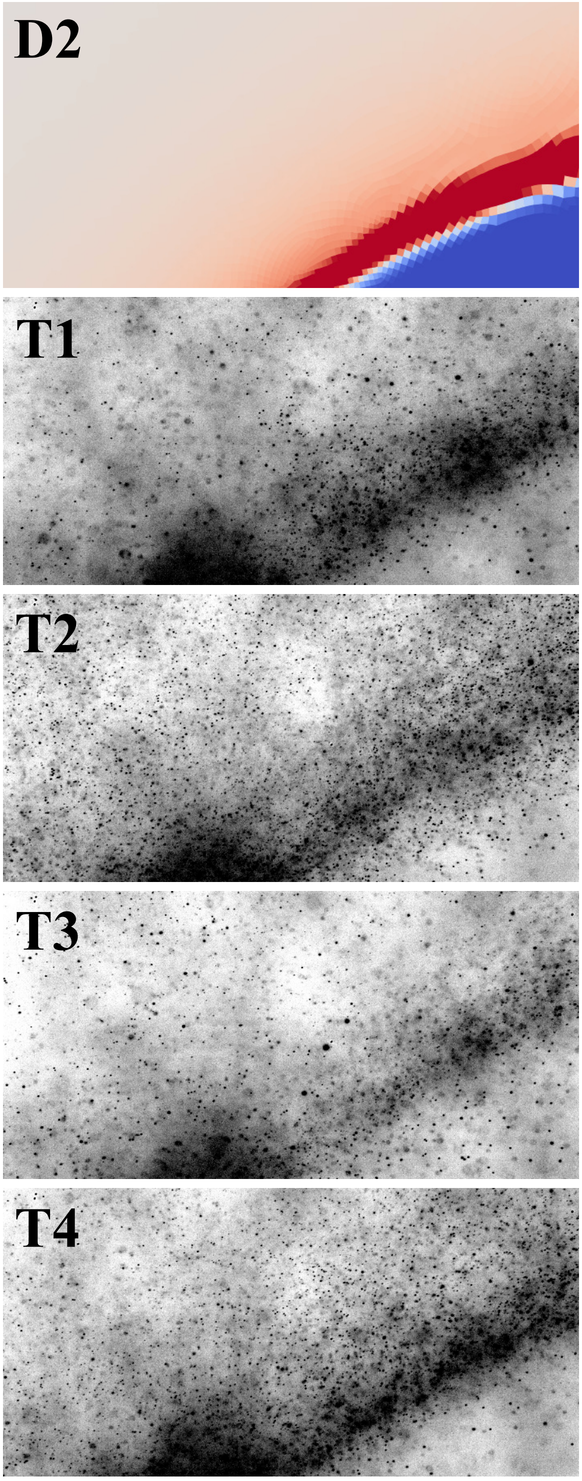

Figure 7. Comparison of pictures obtained from the experiments with the concentration of particles of D2.

larger particles tend to travel horizontally in the streamwise direction largely unabated, whereas smaller particles exhibit shear-layer flapping analogous to that of the shear layer itself. This phenomenon cannot be captured with the current particle solver, since it uses the averaged flow field as an input for the calculations (Fig. 3). Further investigations on the effect of the non-stationary flow in the averaged particle concentrations will eventually be carried.

The current observations display some expected difficulties for the future quantification of particle sizes, velocities and trajectories, since cases with large LWC and low MVDs would tend to present vast amounts of overlapping particles. Therefore, cases such as T3 are encouraged for analysis due to the low amounts of present particles, although it is noted that severely increasing the MVD may result in the suppression of small particles, taking away the notable visualization of the region of high particle concentration, since numerical simulations show that these regions are mostly populated with small-sized particles. Future experiments are expected for further analysis of the particle dynamics.

OUTLOOK

An experimental setup amenable for depth-for-defocus particle tracking was developed to capture the dynamics of a polydisperse cloud interacting with a shear layer separating off of a vertical flat plate normal to the flow. Initial numerical simulations were performed, indicating the location just above or below the point of separation as an effective field-of-view for measurements, exhibiting high accelerations and particle concentrations, and rich particle dynamics that act to reorganize the original PSD. Initial particle-shadow images exhibited a strongly concentrated band angled away from the centreline, with increasing severity at lower MVD, consistent with the numerical simulations. Real-time footage suggested reorganization of the cloud in the presence of the flapping shear layer, with larger particles proceeding through the shear layer relatively unabated, whereas smaller particles generally complied with shear layer motions. From the different tested parameters, it was established that future measurements should focus in particle clouds with low LWC and high MVD in order to guarantee clarity and avoid overlapping of particles for the future extraction of particle size, velocity and trajectories.

REFERENCES

Bagheri, Meysam & Sabzpooshani, Majid 2020 On the importance of the history force in dispersion of particles in von kármán vortex street. *Advanced Powder Technology* **31** (9), 3897–3909.

Lacour, Corine, Durox, Daniel, Ducruix, Sebastien & Massot, Marc 2011 Interaction of a polydisperse spray with vortices. *Experiments in fluids* **51** (2), 295–311.

Maxey, Martin R & Riley, James J 1983 Equation of motion for a small rigid sphere in a nonuniform flow. *The Physics of Fluids* **26** (4), 883–889.

Menter, Florian R 1994 Two-equation eddy-viscosity turbulence models for engineering applications. *AIAA Journal* **32** (8), 1598–1605.

Michaelides, E.E., Sommerfeld, M. & van Wachem, B. 2022 Multiphase flows with droplets and particles .

Monchaux, Romain, Bourgoin, Mickael & Cartellier, Alain 2012 Analyzing preferential concentration and clustering of inertial particles in turbulence. *International Journal of Multiphase Flow* **40**, 1–18.

Pushkin, Dmitri O, Melnikov, Denis E & Shevtsova, Valentina M 2011 Ordering of small particles in one-dimensional coherent structures by time-periodic flows. *Physical review letters* **106** (23), 234501.

Sotomayor-Zakharov, D & Bansmer, S 2021 Finite-volume eulerian solver for simulation of particle-laden flows for icing applications. *Computers & fluids* **228**, 105009.

Sotomayor-Zakharov, D, Sobotta, B & Knop, I 2023 A dynamic collection efficiency formulation implemented in the icing code DICEPS. *International Journal of Heat and Mass Transfer* **217**, 124590.

Xu, R., Huang, Z., Gong, W., Zhou, W. & Tropea, C. 2024 Depth from defocus technique for irregular particle images. *Measurement, Volume 238* .

Yao, Jun, Zhao, Yanlin, Hu, Guilin, Fan, Jianren & Cen, Kefa 2009 Numerical simulation of particle dispersion in the wake of a circular cylinder. *Aerosol Science and Technology* **43** (2), 174–187.

Zhou, W., Tropea, C., Chen, B., Xu Luo, Y. Z. & Cai, X. 2020 Spray drop measurements using depth from defocus. *Measurement Science and Technology 31* .